Optics Letters

High-efficiency second-harmonic generation of low-temporal-coherent light pulse

Lailin Ji,[1,†] Xiaohui Zhao,[1,†] Dong Liu,[1,†] Yanqi Gao,[1,*] Yong Cui,[1] Daxing Rao,[1] Wei Feng,[1] Fujian Li,[1] Haitao Shi,[1] Jiani Liu,[1] Xiaoli Li,[1] Lan Xia,[1] Tao Wang,[1] Jia Liu,[1] Pengyuan Du,[1] Xun Sun,[2] Weixin Ma,[1] Zhan Sui,[1] and Xianfeng Chen[3]

[1]Shanghai Institute of Laser Plasma, China Academy of Engineering Physics, 1129 Chenjiashan Road, Shanghai 201800, China
[2]State Key Laboratory of Crystal Materials, Shandong University, Jinan 250100, China
[3]School of Physics and Astronomy, Shanghai Jiao Tong University, 800 Dongchuan Road, Shanghai 200240, China
*Corresponding author: liufenggyq@siom.ac.cn

Received 21 June 2019; revised 6 August 2019; accepted 7 August 2019; posted 7 August 2019 (Doc. ID 370629); published 28 August 2019

The nonlinear frequency conversion of low-temporal-coherent light holds a variety of applications and has attracted considerable interest. However, its physical mechanism remains relatively unexplored, and the conversion efficiency and bandwidth are extremely insufficient. Here, considering the instantaneous broadband characteristics, we establish a model of second-harmonic generation (SHG) of a low-temporal-coherent pulse and reveal its differences from the coherent conditions. It is found that the second-harmonic spectrum distribution is proportional to the self-convolution of that of a fundamental wave. Because of this, we propose a method for realizing low-temporal-coherent SHG with high efficiency and broad bandwidth, and experimentally demonstrate a conversion efficiency up to 70% with a bandwidth of 3.1 THz (2.9 nm centered at 528 nm). To the best of our knowledge, this is the highest efficiency and broadest bandwidth of low-temporal-coherent SHG to date. Our research opens the door for the study of low-coherent nonlinear optical processes.

https://doi.org/10.1364/OL.44.004359

One of the most challenging issues in laser-driven inertial confinement fusion (ICF) is the suppression of laser-plasma instabilities (LPIs), when an intense laser transmits through a surrounding plasma [1–3]. The key to solving this problem is decoherence of a high coherent drive laser to reduce instabilities caused by nonlinear processes [4,5], such as self-focusing, stimulated Raman scattering, stimulated Brillouin scattering, and crossed-beam energy transfer [6–8]. At present, beam smoothing techniques, which reduce the temporal and spatial coherence of laser, are the main solution and have been widely used in laser-fusion facilities around the world [9–11]. In general, the bandwidth of the laser for ICF, as limited by modulators, is about 100 GHz [12]. The frequency components vary periodically with time. These factors severely limit the smoothing speed and smoothing effect of laser beam. Plenty of experiments and analysis indicate that the adverse effects of LPI under fusion conditions are difficult to effectively overcome using current beam smoothing techniques [13–15]. A more straightforward solution is to use broadband low-temporal-coherent laser sources ($\Delta\nu/\nu > 1\%$) for ignition [16,17]. These laser sources have broader bandwidths, more spectrum components, and lower coherence for achieving a better smoothing effect. This method is expected to alleviate the LPI problem that has plagued the fusion field for many years. For the LPIs, shorter laser wavelengths can improve the coupling efficiency of the laser-plasma interaction and reduce harmful processes. Currently, most fusion facilities operate at the third harmonic (351 nm) of Nd:glass lasers. However, damages caused by ultraviolet lasers severely limit the facility output ability and greatly increase the operation cost. In addition, the narrow acceptance bandwidth of the existing third-harmonic generation method restricts the effect of the current beam smoothing technologies. The low-coherent second-harmonic (SH) drive will greatly alleviate, or even solve the above problems [18]. Hence, frequency conversion techniques for a broadband low-temporal-coherent laser may open the door to use the SH laser for ignition [19].

Typical applications of SH generation (SHG) and sum-frequency generation (SFG) of narrowband coherent lasers in ICF facilities can have a conversion efficiency up to 80%. With the development of ultrashort pulses, frequency conversion of broadband coherent pulses (chirped and compressed pulses) has been widely studied. The greatest difficulty is satisfying the phase-matching (PM) and group-velocity matching (GVM) conditions simultaneously, which determine the conversion efficiency and spectral bandwidth of nonlinear processes. The multi-crystal scheme [20], angular spectral dispersion method [21], partially deuterated (DKDP) crystal [22], and adiabatic processes [23,24] have been developed for the SHG of broadband coherent pulses. The highest SH conversion efficiency (η) has reached 75% with a bandwidth ($\Delta\lambda$) of about 3 nm under an extremely high intensity of about 380 GW/cm^2 [25]. For broadband coherent pulses, achieving high-efficiency harmonic conversion under moderate

intensities (~GW/cm^2) is still a challenge. Recently, the SHG of a low-coherent pulse has attracted considerable interest. Some pioneer theoretical and experimental studies on SHG of low-spatial-coherent pulses have been carried out [26,27], and the obtained conversion efficiency is about 35% with a divergence of 3.5 mrad [28]. However, studies for the SHG of low-temporal-coherent pulses are relatively insufficient, and the physical mechanism is still not conclusive.

In this Letter, we study the physical mechanism of the low-temporal-coherent SHG process. The difference from its coherent counterpart is clarified from the perspective of statistical optics. The distribution of the SH spectrum is theoretically predicted, i.e., a self-convolution of the fundamental wave (FW) spectrum distribution. Furthermore, we experimentally demonstrate the realization of low-temporal-coherent broadband SHG with a conversion efficiency up to 70%. The spectral evolution characteristics are consistent with the proposed theoretical modeling. Our research has great significance for the study of low-temporal-coherence nonlinear optical processes.

The low-temporal-coherent pulses discussed here, unless otherwise specified, are spatially coherent. Generally, the low-temporal-coherent light pulse has an instantaneous broadband characteristics. Different from compressed [Fig. 1(a)], chirped [Fig. 1(b)], or modulated pulses [Fig. 1(c)], the frequency components of low-temporal-coherent pulses [Fig. 1(d)] have a wide distribution at any time within the pulse duration. Under the conditions of simultaneous PM and GVM, multiple physical processes will take place in the nonlinear medium. The schematic of instantaneous broadband SHG is shown in Fig. 1(e), where processes (1), (3), and (4) are degenerate SHG of FWs; process (2) denotes SFG of two FW waves with different frequencies. It can be inferred that SH at a specific wavelength can be generated by both degenerate SHG and SFG from different spectral components of the FW. The distribution of the SH spectrum should be determined by the spectrum and statistical characteristics of the FW.

To analyze the SHG process of a low-temporal-coherent pulse, statistical optics is introduced to calculate the intensity of the SH wave. Under the PM condition, the complex amplitude of the SH electrical field can be calculated as $E_{2\omega} = \sqrt{\eta} E_\omega^2/|E_\omega|$, where E_ω is the complex amplitude of the FW and η is the conversion efficiency. Thus, the temporal autocorrelation function of SH is

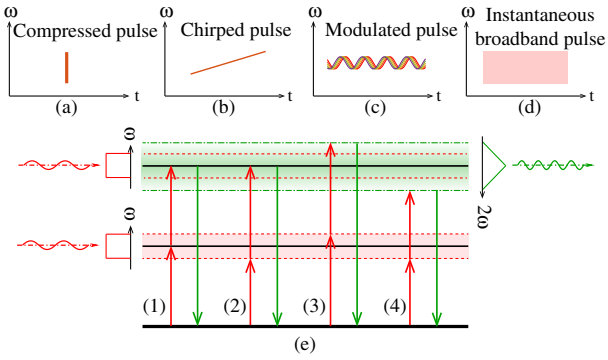

Fig. 1. Spectrum distribution of (a) a compressed pulse, (b) a chirped pulse, (c) a modulated pulse, and (d) an instantaneous broadband pulse. (e) Schematic of different strategies for an instantaneous broadband SHG.

$$\gamma_{2\omega}(\tau) = \langle E_{2\omega}^*(t) E_{2\omega}(t') \rangle \propto \langle E_\omega^{2*}(t) E_\omega^2(t') \rangle, \quad (1)$$

where t and t' are two moments within the pulse duration, $\tau \equiv t' - t$, and the symbol $\langle \cdot \rangle$ represents an average for infinite time. According to the Wiener–Khinchin theorem, the spectrum is the Fourier transform of the temporal autocorrelation function, so the spectrum of SH can be derived from Eq. (1) as

$$I_{2\omega}(\nu) = \Im\{\gamma_{2\omega}(\tau)\} \propto \langle |E_\omega(\nu) \otimes E_\omega(\nu)|^2 \rangle. \quad (2)$$

The frequency-domain electric field $E_\omega(\nu) = \sqrt{I_\omega(\nu)} \exp[i\phi(\nu)]$ is the Fourier transform of $E_\omega(t)$. $I_\omega(\nu)$ and $\phi(\nu)$ are the spectral intensity and spectral phase of the FW, respectively. For different sources, $E_\omega(\nu)$ has different statistical characteristics and different spectral profiles. For the instantaneous broadband source, its amplitude and spectral phase is statistically independent, and the phase is evenly distributed in the whole range of $[-\pi, \pi]$. Then we can get the relationship between the spectral intensity of SH and that of the FW as follows:

$$I_{2\omega}(\nu) \propto I_\omega(\nu) \otimes I_\omega(\nu). \quad (3)$$

Equation (3) concludes that the spectrum of SH is proportional to the self-convolution of the FW spectrum. It is different from the coherent SHG process, in which the frequency-domain electric field of SH is proportional to the self-convolution of that of the FW.

For an experimental demonstration, a superluminescent diode pulse source amplified by a Nd:phosphate glass rod laser system was chosen as the pumped laser. The time-domain waveform and spectral distribution of the delivered pulses is independent [29], showing an instantaneous broadband characteristics [Fig. 1(d)]. The spatial profile of the beam is close to a 12th-order super-Gaussian with a size of 42 mm × 42 mm. It delivers an intensity up to 0.75 GW/cm^2 within a 3 ns pulse duration. The output spectral width is approximate 10.2 nm centered at 1057 nm. The coherent time was experimentally measured to be 318 fs, far shorter than the pulse duration, inferring that the pulse has low temporal coherence. Moreover, the near- and far-field beam profiles indicate that the light source has good spatial coherence.

For simultaneously satisfying the PM and GVM conditions, a 15% DKDP crystal with a cutting angle $\theta = 41°$ for a type-I PM scheme was utilized, whose central PM wavelength is 1057 nm. Based on the numerical simulation of the nonlinear coupled-wave equations, the crystal length was optimized to be 32 mm. It provides an acceptance bandwidth of about 12 nm at the retracing point, when the SHG falls into the regime of saturation. The cross-sectional dimension of the crystal is 70 mm × 70 mm. After the nonlinear crystal, three dichroic mirrors (M1–M3) were used to separate the SH wave and the residual FW, as shown in Fig. 2. The energy of SH was measured by an energy meter. The spectrometer behind the M1 is utilized to detect the spectrum of the FW and SH. Behind M2, the leaked SH wave was split into two beams, then focused by lenses L1 and L2 for the detection of a far-field spatial profile and temporal waveform, respectively.

Figure 3 presents the primary experimental results. The FW is a square waveform with a pulse duration of 3 ns [Fig. 3(a)], measured by a 4 GHz oscilloscope. The time waveform of SH is the same as that of the FW. The spectrum of the FW [Fig. 3(b)] has a rectangular-shaped distribution. The full width at half-maximum (FWHM) of the spectrum is 10.2 nm

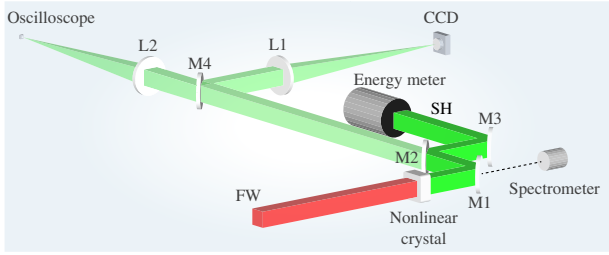

Fig. 2. Experimental setup. M1–M3, SH beam splitters; M4, beam splitter. L1 and L2 are focusing lenses with a focal length of 1 m, a CCD, and an oscilloscope measure the far-field profile and temporal waveform of SH.

(2.7 THz). The spectrum of SH has a triangular profile with a bandwidth (FWHM) of 2.9 nm (3.1 THz). To the best of our knowledge, this is the broadest bandwidth of a low-temporal-coherent SH pulse. In addition, the spectrum distribution in Fig. 3(b) shows that the spectrum of SH is consistent with the self-convolution of that of the FW, which is in good agreement with the theoretical prediction.

Figure 3(c) shows the relationship of the SH conversion efficiency with respect to the FW energy. The conversion efficiency was calculated by dividing the SH energy by the incident FW energy (measured before the nonlinear crystal, not shown in Fig. 2), and compensating for the loss by the three dichroic mirrors (~3%). In our experiments, the highest conversion efficiency reached 70% at a moderate FW intensity of 0.75 GW/cm^2 [corresponding to 37 J FW pulse input in Fig. 3(c)]. To the best of our knowledge, this is the highest conversion efficiency of low-temporal-coherent SHG. Theoretically, at the conventional power density of a high-power laser facility for ICF (3–4 GW/cm^2), it can achieve a conversion efficiency about 80%, which is almost the same with the highest conversion efficiency on a narrowband coherent laser facility. The conversion efficiency is a pivotal parameter for some applications, especially ICF, which decides the highest available driver energy. The curves in Fig. 3(c) are the simulation results based on the nonlinear coupled equation,

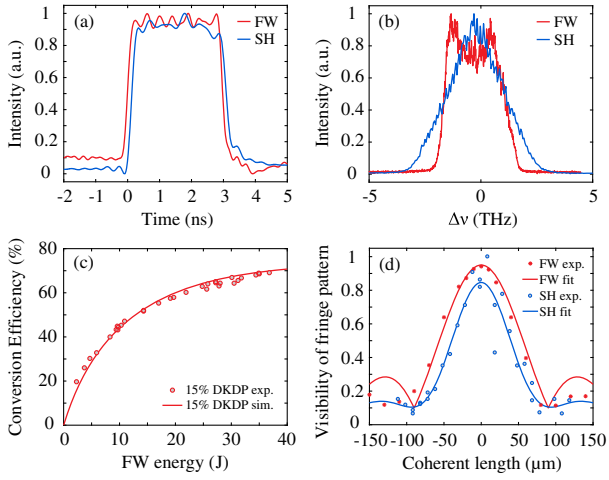

Fig. 3. Experimental results of SHG: (a) temporal waveforms and (b) spectra of the FW and SH, respectively; (c) SH conversion efficiency; (d) coherence length measurement for the FW and SH.

taking into account the statistical characteristics of the instantaneous broadband source. The simulation and experimental results are in agreement with each other.

Experimentally, the temporal coherence length of the FW and SH was measured by a Michelson interferometer, and the result was shown in Fig. 3(d). Theoretically, the contrast function $\Gamma(\tau)$ is the module of the temporal autocorrelation function $\gamma_{2\omega}(\tau)$. From Eq. (2), one can derive that $\Gamma(\tau) = |\Im^{-1}\{I_{2\omega}(\nu)\}|$. The spectrum of SH has a triangular distribution in our experiment, so that the contrast function is in the form of $\mathrm{sinc}^2(\Delta\nu\tau)$, where $\Delta\nu$ is the FWHM of the SH spectrum. Similarly, the contrast function of the FW is in the form of $\mathrm{sinc}(\Delta\nu_1\tau)$, where $\Delta\nu_1$ is the FWHM of the FW spectrum. The relationship of the visibility of fringe pattern versus the optical path difference is in good agreement with the theoretical prediction. The coherence time of SH is 300 fs, which is similar to that of the FW (318 fs). It is far shorter than the pulse duration, as shown in Fig. 3(a), demonstrating that the low coherent characteristics have been transferred to the SH during the SHG process.

Far-field focusing characteristics of the FW and SH are shown in Fig. 4. For the SH wave, more than 70% of the energy is within the area of 1.7 times the diffraction limit (DL) and more than 95% energy is in the area of 3.7 times DL, which is slightly degraded, as compared to that of the FW. This shows that the low-temporal-coherent pulse utilized in experiments is spatial coherent, in accordance to the assumptions of the model in this Letter. After the conversion process, the SH pulse holds an excellent far-field performance, which presents a good focusing capability required by practical applications.

To further verify our theoretical inference on the physical mechanism of the low-temporal-coherent nonlinear frequency conversion process, the evolution of the spectral characteristics was also investigated. We shaped the spectrum of the FW to a bimodal structure with peak center wavelengths of 1052 and 1060 nm, respectively, as shown in Fig. 5(a). Also, its waveform was maintained to be square in the time domain. The theoretical self-convolution of the FW spectrum is shown in Fig. 5(b), which has three peaks with center wavelengths of 526, 528, and 530 nm. Figure 5(c) present the evolutions of the SH spectrum varying with the incident angle θ in the 15% DKDP, where θ is defined as the external rotation angle with respect to the o-axis of the crystal.

At the angle of 0 μrad, corresponding to the retracing point of the PM condition, the spectrum of SH has a similar shape with the theoretically prediction in Fig. 5(b), which confirms the self-convolution relationship described in Eq. (3). Although the frequency components of the FW are filtered at around 1056 nm, the SH still has a spectral peak at 528 nm. It verified

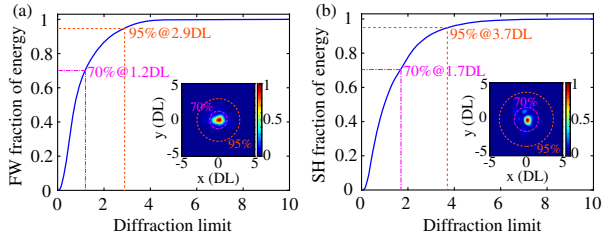

Fig. 4. Energy concentration rate curve of the (a) FW and (b) SH focusing by lenses with a focal length of 1.026 m. The insets are the far-field profile of the FW and SH, respectively.

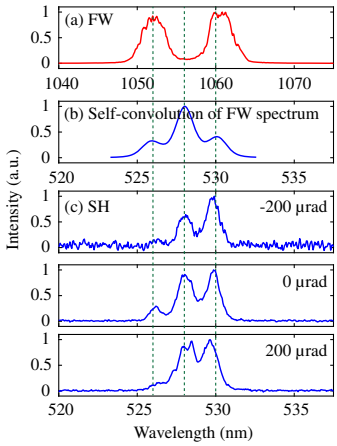

Fig. 5. Evolution of the SH spectrum varying with the incident angles: (a) shaped spectrum of the FW, (b) self-convolution of the FW spectrum, and (c) the SH spectrum using 15% DKDP crystal at different angles.

that in the low-temporal-coherent SHG process, the harmonic waves are produced by not only the degenerate SHG, but also the crossed SFG processes.

Moreover, in experiment, the acceptance bandwidth of a nonlinear crystal is not infinite, which is equivalent to a filtering process. We verified this filtering process by adjusting the crystal angles to change the center wavelength of the PM. The PM angle is monotonic for wavelength. Varying with the incident angles, the peak of the SH spectrum is shifted. The above experimental results not only demonstrate our theoretical analysis, but also predict a broader-band SHG by modulating the spectrum of the FW.

We investigated the novel physical mechanism of low-temporal-coherent SHG process based on the instantaneous broadband characteristics. The essential difference with harmonic processes of coherent light is that the convolution relationship is between the spectrum distribution of SH and the FW, not the frequency-domain electric field. The method for high-efficiency low-temporal-coherent SHG with a broadband was proposed. The conversion efficiency in our experiment was up to 70% (at GW/cm^2), and the bandwidth is 3.1 THz (2.9 nm). The low-temporal coherence characteristics were kept during the nonlinear process. Moreover, the spectrum evaluation relationship during the SHG process was demonstrated experimentally, which is consistent with the theoretical prediction. The analysis is also applicable to third- and even higher-order harmonic generation processes of low-temporal-coherent light. Our research will have a further impact on the study of the nonlinear optical process of low-coherence light.

Funding. Science Challenge Project (TZ2016005); National Natural Science Foundation of China (11604317, 11604318, 11804321).

†These authors contributed equally to this Letter.

REFERENCES

1. R. Betti and O. A. Hurricane, Nat. Phys. **12**, 435 (2016).
2. O. A. Hurricane, D. A. Callahan, D. T. Casey, P. M. Celliers, C. Cerjan, E. L. Dewald, T. R. Dittrich, T. Döppner, D. E. Hinkel, L. F. B. Hopkins, J. L. Kline, S. LePape, T. Ma, A. G. MacPhee, J. L. Milovich, A. Pak, H. S. Park, P. K. Patel, B. A. Remington, J. D. Salmonson, P. T. Springer, and R. Tommasini, Nature **506**, 343 (2014).
3. J. Lindl, O. Landen, J. Edwards, and E. Moses, Phys. Plasmas **21**, 020501 (2014).
4. C. Labaune, Nat. Phys. **3**, 680 (2007).
5. S. H. Glenzer, D. H. Froula, L. Divol, M. Dorr, R. L. Berger, S. Dixit, B. A. Hammel, C. Haynam, J. A. Hittinger, and J. P. Holder, Nat. Phys. **3**, 716 (2007).
6. J. D. Lindl, P. Amendt, R. L. Berger, S. G. Glendinning, S. H. Glenzer, S. W. Haan, R. L. Kauffman, O. L. Landen, and L. J. Suter, Phys. Plasmas **11**, 339 (2004).
7. P. Michel, L. Divol, E. A. Williams, S. Weber, C. A. Thomas, D. A. Callahan, S. W. Haan, J. D. Salmonson, S. Dixit, D. E. Hinkel, M. J. Edwards, B. J. MacGowan, J. D. Lindl, S. H. Glenzer, and L. J. Suter, Phys. Rev. Lett. **102**, 025004 (2009).
8. J. D. Moody, P. Michel, L. Divol, R. L. Berger, E. Bond, D. K. Bradley, D. A. Callahan, E. L. Dewald, S. Dixit, and M. J. Edwards, Nat. Phys. **8**, 344 (2012).
9. M. L. Spaeth, K. R. Manes, M. Bowers, P. Celliers, J.-M. D. Nicola, P. D. Nicola, S. Dixit, G. Erbert, J. Heebner, and D. Kalantar, Fusion Sci. Technol. **69**, 366 (2016).
10. C. Dorrer, A. Consentino, R. Cuffney, I. A. Begishev, E. M. Hill, and J. Bromage, Opt. Express **25**, 26802 (2017).
11. S. Jiang, F. Wang, Y. Ding, S. Liu, J. Yang, S. Li, T. Huang, Z. Cao, Z. Yang, X. Hu, W. Miao, J. Zhang, Z. Wang, G. Yang, Y. Rongqing, Q. Tang, L. Kuang, Z. Li, Y. Dong, and B. Zhang, Nucl. Fusion **59**, 032006 (2018).
12. C. A. Haynam, P. J. Wegner, J. M. Auerbach, M. W. Bowers, S. N. Dixit, G. V. Erbert, G. M. Heestand, M. A. Henesian, M. R. Hermann, K. S. Jancaitis, K. R. Manes, C. D. Marshall, N. C. Mehta, J. Menapace, E. Moses, J. R. Murray, M. C. Nostrand, C. D. Orth, R. Patterson, R. A. Sacks, M. J. Shaw, M. Spaeth, S. B. Sutton, W. H. Williams, C. C. Widmayer, R. K. White, S. T. Yang, and B. M. V. Wonterghem, Appl. Opt. **46**, 3276 (2007).
13. D. S. Montgomery, Phys. Plasmas **23**, 055601 (2016).
14. M. J. Rosenberg, A. A. Solodov, J. F. Myatt, W. Seka, P. Michel, M. Hohenberger, R. W. Short, R. Epstein, S. P. Regan, E. M. Campbell, T. Chapman, C. Goyon, J. E. Ralph, M. A. Barrios, J. D. Moody, and J. W. Bates, Phys. Rev. Lett. **120**, 055001 (2018).
15. P. Michel, L. Divol, E. L. Dewald, J. L. Milovich, M. Hohenberger, O. S. Jones, L. B. Hopkins, R. L. Berger, W. L. Kruer, and J. D. Moody, Phys. Rev. Lett. **115**, 055003 (2015).
16. D. Eimerl, E. M. Campbell, W. F. Krupke, J. Zweiback, W. L. Kruer, J. Marozas, J. Zuegel, J. Myatt, J. Kelly, and D. Froula, J. Fusion Energy **33**, 476 (2014).
17. J. W. Bates, J. F. Myatt, J. G. Shaw, R. K. Follett, J. L. Weaver, R. H. Lehmberg, and S. P. Obenschain, Phys. Rev. E **97**, 061202 (2018).
18. M. Chambonneau, J.-L. Rullier, P. Grua, and L. Lamaignère, Opt. Express **26**, 21819 (2018).
19. L. J. Suter, S. Glenzer, S. Haan, B. Hammel, K. Manes, N. Meezan, J. Moody, M. Spaeth, L. Divol, K. Oades, and M. Stevenson, Phys. Plasmas **11**, 2738 (2004).
20. D. Eimerl, IEEE J. Quantum Electron. **23**, 1361 (1987).
21. M. D. Skeldon, R. S. Craxton, T. Kessler, W. Seka, R. W. Short, S. Skupsky, and J. M. Soures, IEEE J. Quantum Electron. **28**, 1389 (1992).
22. M. S. Webb, D. Eimerl, and S. P. Velsko, J. Opt. Soc. Am. B **9**, 1118 (1992).
23. H. Suchowski, G. Porat, and A. Arie, Laser Photonics Rev. **8**, 333 (2014).
24. E. Rozenberg and A. Arie, Opt. Lett. **44**, 3358 (2019).
25. D. Hillier, C. Danson, S. Duffield, D. Egan, S. Elsmere, M. Girling, E. Harvey, N. Hopps, M. Norman, S. Parker, P. Treadwell, D. Winter, and T. Bett, Appl. Opt. **52**, 4258 (2013).
26. Y. Cai and U. Peschel, Opt. Express **15**, 15480 (2007).
27. V. G. Dmitriev, M. V. Osipov, V. N. Puzyrev, A. T. Sahakyan, A. N. Starodub, and B. L. Vasin, J. Phys. B **45**, 165401 (2012).
28. B. L. Vasin, Y. V. Korobkin, M. V. Osipov, V. N. Puzyrev, A. T. Sahakyan, A. N. Starodub, and S. I. Fedotov, Bull. Lebedev Phys. Inst. **40**, 205 (2013).
29. Y. Cui, Y. Gao, D. Rao, D. Liu, F. Li, L. Ji, H. Shi, J. Liu, X. Zhao, W. Feng, L. Xia, J. Liu, X. Li, T. Wang, W. Ma, and Z. Sui, Opt. Lett. **44**, 2859 (2019).